

RESEARCH ARTICLE | MAY 06 2022

Tuning the structural, magnetic, and transport properties of Mn₃Ga alloys

Linxuan Song ; Weike Li ; Senhao Lv; Xuekui Xi ; Dongliang Zhao; Jun He ; Wenhong Wang  



J. Appl. Phys. 131, 173903 (2022)

<https://doi.org/10.1063/5.0087415>



Articles You May Be Interested In

Tunable magnetic and transport properties of Mn₃Ga thin films on Ta/Ru seed layer

J. Appl. Phys. (March 2018)

Epitaxial growth of the cubic L2₁-Mn_{2.6}Ga Heusler alloy on MgO(001)

Appl. Phys. Lett. (April 2020)

Large room temperature anomalous Hall effect in c axis oriented non-collinear antiferromagnetic Mn₃Ga thin films with ferrimagnetic Mn₃Ga inclusion

Appl. Phys. Lett. (September 2025)



Nanotechnology &
Materials Science



Optics &
Photonics



Impedance
Analysis



Scanning Probe
Microscopy



Sensors



Failure Analysis &
Semiconductors



Unlock the Full Spectrum.
From DC to 8.5 GHz.

Your Application. Measured.

[Find out more](#)

 Zurich
Instruments

Tuning the structural, magnetic, and transport properties of Mn₃Ga alloys

Cite as: J. Appl. Phys. 131, 173903 (2022); doi: 10.1063/5.0087415

Submitted: 14 February 2022 · Accepted: 24 April 2022 ·

Published Online: 6 May 2022



View Online



Export Citation



CrossMark

Linxuan Song,^{1,2} Weike Li,² Senhao Lv,¹ Xuekui Xi,² Dongliang Zhao,¹ Jun He,^{1,a)} and Wenhong Wang^{3,a)}

AFFILIATIONS

¹Division of Functional Material Research, Central Iron and Steel Research Institute, No. 76 Xueyuan South Road, Haidian District, Beijing 100081, China

²Institute of Physics, Chinese Academy of Sciences, Beijing 100190, China

³School of Electronic and Information Engineering, Tiangong University, Tianjin 300387, China

^{a)}Authors to whom correspondence should be addressed: hejun@cisri.com.cn and wenhongwang@tiangong.edu.cn

ABSTRACT

Mn₃Ga alloys with different crystal modifications, including a disordered L1₂-type cubic structure, a D0₂₂-tetragonal structure, and a D0₁₉-hexagonal structure showing two isomorphic heteromagnetic phases, ϵ -phase and η -phase, were investigated systematically. We found that the disordered cubic phase and the hexagonal ϵ -phase can be synthesized with Mn compositions ranging from 70 to 75 at. % by rapid melt-spinning. Moreover, the disordered cubic phase could transform to the tetragonal phase after being subjected to low-temperature post-annealing. Most importantly, we found that proper postannealing conditions can enable these different crystal modification phases to transform to the hexagonal η -phase. As a result, the two isomorphic heteromagnetic hexagonal phases are clearly distinguished, and their interesting magnetic and transport properties are discussed.

Published under an exclusive license by AIP Publishing. <https://doi.org/10.1063/5.0087415>

I. INTRODUCTION

Mn–Ga binary alloys can be synthesized with three different crystal modifications and have attracted increasing attention for decades as potential candidates for spintronic applications. Importantly, the magnetic ordering of these modifications varies from collinear antiferromagnetic (AFM) ordering in the disordered L1₂-type cubic phase^{1,2} to ferrimagnetic ordering in the tetragonal case³ to noncollinear AFM ordering in the D0₁₉-type hexagonal phase.⁴

In fact, the disordered cubic phase corresponds to the γ Mn-phase in the Mn–Ga binary diagram. Based on previous experiments,^{1,5} as shown in Fig. 1(a), the substitutional disorder causes the Mn atoms with antiparallel spins cancel each other, which induces AFM ordering. A rapid quenching treatment can facilitate the formation of a high-temperature phase, which can be achieved by rapid melt-spinning technique. By using first-principles calculations, Kharel¹ and co-workers discussed disordered atomic site occupation in the high-temperature phase. It is worth noting that the disordered cubic phase can transform to

the tetragonal phase and even the hexagonal phase after a proper heat treatment.^{1,3}

Moreover, in the D0₂₂-tetragonal structure,^{6–8} as shown in Fig. 1(c), Mn I and Mn II atoms occupy two different positions with antiparallel spins, forming ferrimagnetic ordering.⁴ We *et al.*⁹ found that due to its large magnetocrystalline anisotropy, the tetragonal phase can be a candidate for rare-earth free permanent magnets and that the coercivity can reach 21.4 kOe for a Mn₃Ga pressed powder disk sample. Furthermore, the electronic structure calculation indicates a ground state with 88% spin polarization at the Fermi energy of tetragonal Mn₃Ga,^{10,11} while experiments show that epitaxial c-axis films exhibit spin polarization as high as 58%,¹² which implies that tetragonal Mn₃Ga is promising for applications in spintronic devices.

Previous studies have shown that the hexagonal phase may be obtained from cubic Mn₃Ga by postannealing.¹ Actually, the hexagonal structure has two phase regions in the Mn–Ga binary diagram,⁵ the so-called ϵ -phase¹³ region and the η -phase region. However, because they have a similar lattice constant, the ϵ -phase

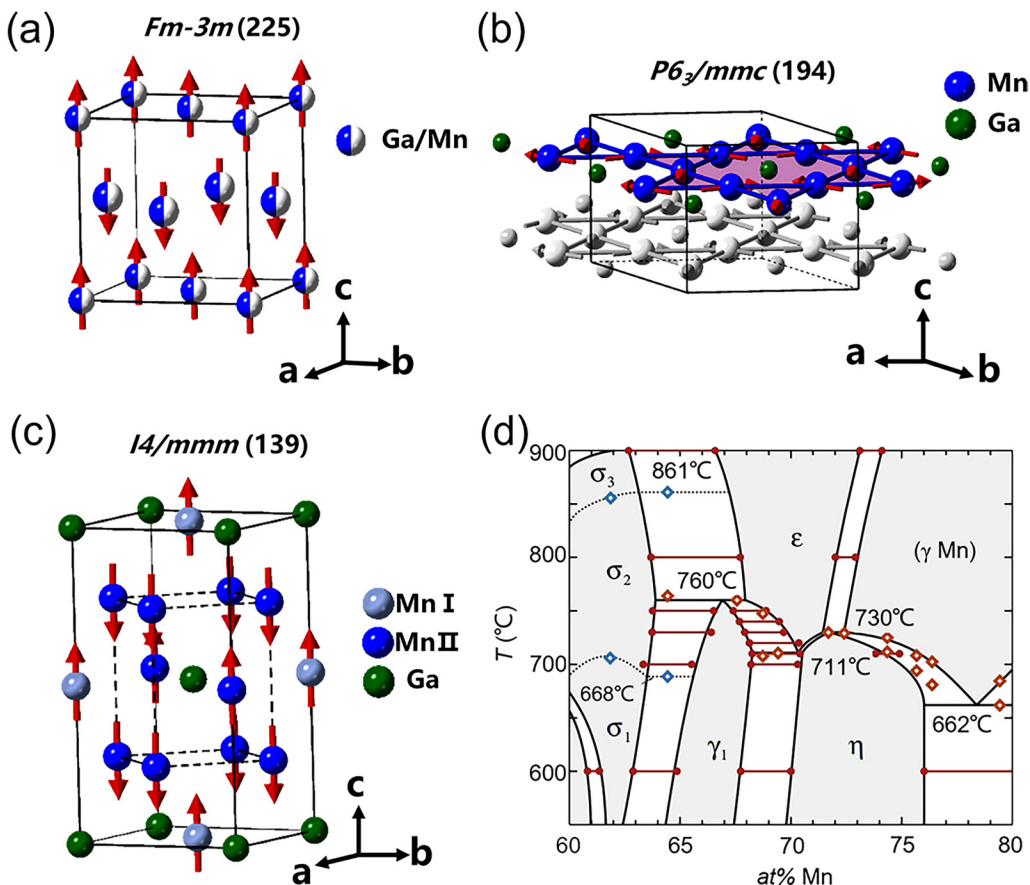


FIG. 1. The crystalline and magnetic structures of different Mn_3Ga alloys: (a) cubic phase (γ -Mn phase), (b) tetragonal phase, and (c) hexagonal phase (η -phase). (d) Partial Mn-Ga binary phase diagram in the range from 70 to 75 at. % Mn.⁵ (d) Reproduced with permission from Kazuhiro Minakuchi *et al.*, J. Alloys Compd. **537**, 332 (2012). Copyright 2012 Elsevier.

01 October 2025 05:34:38

has been considered to be a disordered η -phase and is rarely studied. In our previous work, we observed a clear exchange bias in the ϵ -phase due to the disordered atomic site occupation resulting in the coexistence of AFM and FM phases.¹⁴ The hexagonal η -phase exhibits noncollinear antiferromagnetism, as shown in Fig. 1(b). Three atoms in a plane form a triangular sublattice with a noncollinear 120° in-plane spin order, and their magnetic moments cancel each other in the triangle, forming AFM ordering. It has been found that this special spin configuration can induce Berry curvature in K space, which can result in the large anomalous Hall effect and the anomalous Nernst effect.^{15,16} When the coplanar spin configuration becomes noncoplanar, Mn_3Ga exhibits the topological Hall effect corresponding to the Berry curvature in real space.^{17,18} In addition, for spintronic applications, noncollinear antiferromagnetism Mn_3Ga film also shows some interesting prospects. Mn_3Ga can be applied to the magnetic tunnel junction as a bottom-pinned AFM layer.¹⁹ The magnetic and transport properties of Mn_3Ga films can be tuned by tuning the thickness of the Ta/Ru seed layer.²⁰ Recently, the inverse spin Hall effect and spin

pumping effect were also observed in Mn_3Ga films.²¹ The above-mentioned interesting properties show that the noncollinear antiferromagnetism Mn_3Ga is a promising candidate for applications in future AFM spintronics.

The Mn-Ga binary diagram has been studied in recent years, and the cubic phase has been found to transform to other two phases. The magnetic ordering and exchange interactions in structural modifications of Mn_3Ga are also studied with first-principles calculations.²² However, to the best of our knowledge, how the three different crystal modifications of Mn_3Ga transform into each other has not been systematically discussed. In addition, as shown in Fig. 1(d), in the Mn-Ga binary phase diagram, the η -phase (hexagonal) region has the same composition range as both parts of the γ -phase (cubic) and ϵ -phase (hexagonal) regions in the higher temperature section, which implies that the η -phase is not obtained by a single process. In the present work, we obtain three different phases of Mn_3Ga alloys with Mn compositions ranging from 70 to 75 at. % and synthesize a pure hexagonal η -phase with different Mn compositions over a wide range. The detailed formation conditions

and magnetic and transport properties of these different crystal modifications of Mn_3Ga phases are discussed.

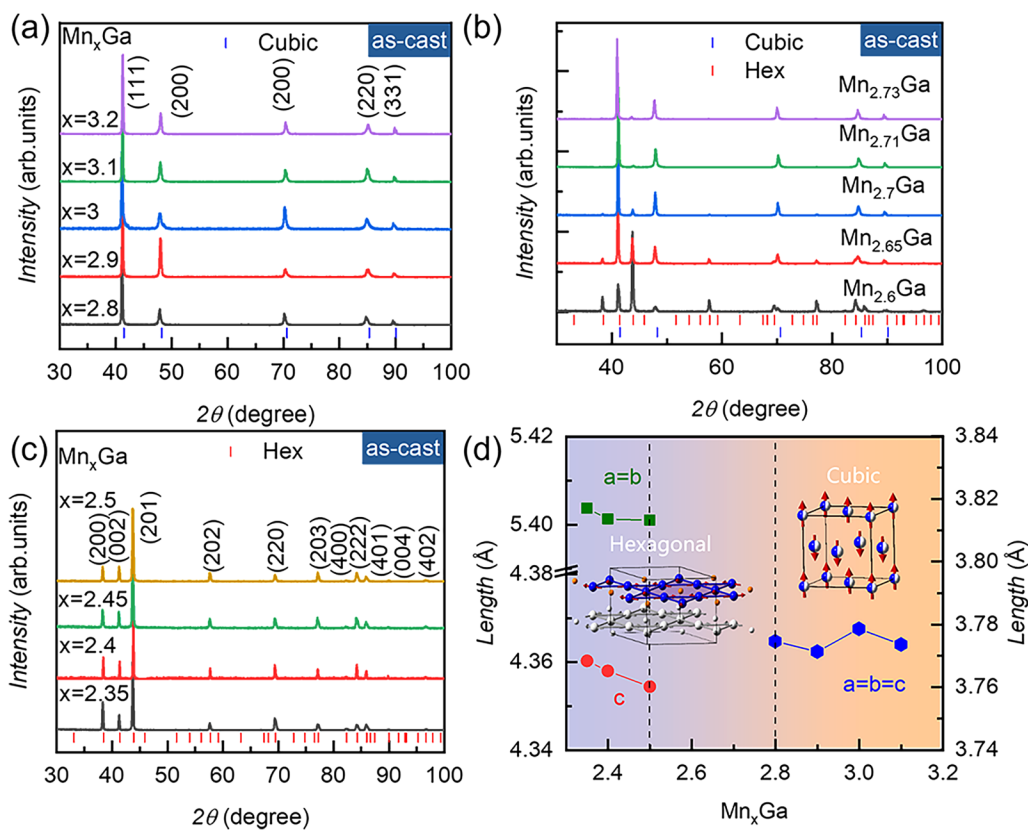
II. EXPERIMENTAL DETAILS

The bulk Mn_3Ga alloys were prepared by arc melting with high-purity Mn (99.999 wt. %) and Ga (99.999 wt. %) under an argon atmosphere. Part of the bulk samples was further melt-spun into ribbons. During melt-spinning, the Mn–Ga ingots were induction melted in a quartz tube and then ejected onto the surface of a rotating copper wheel (the tangential speed of the rotating wheel was kept at 26 m/s), where they rapidly solidified into ribbons. The samples that needed to be annealed were sealed in evacuated quartz tubes and then annealed at proper temperatures. The crystal structure was characterized by x-ray diffraction (XRD) with Cu $K\alpha$ radiation at room temperature and atomic resolution scanning transmission electron microscopy (STEM). The magnetic properties were measured on a magnetic property measuring system (MPMS, Quantum Design) and a vibrating sample magnetometer (VSM, Lake Shore) with high-temperature capabilities. The transport properties were measured on a physical property measuring

system (PPMS, Quantum Design). The transition temperatures were characterized by differential scanning calorimetry (DSC) with heating and cooling rates of 10 K/min.

III. RESULTS AND DISCUSSION

Regions containing all phases of Mn_3Ga occur in the diagram at the same composition. Therefore, it is difficult to obtain a pure phase by only arc melting because the melted alloys first enter the high-temperature phase region and then pass through the low-temperature region in turn during cooling due to the lower cooling rate ($\sim 10^2$ – 10^3 °C/s). However, the cooling rates achievable by melt spinning are on the order of 10^4 – 10^6 °C/s, which can prevent the transition from the phase at the high-temperature section to the other phase at the low-temperature section and more easily yield a pure high-temperature phase. As shown in Fig. 2, the pure γ -phase (cubic) [Fig. 2(a)] and ϵ -phase (hexagonal) [Fig. 2(c)] can be easily obtained over a wide composition range by melt-spinning. Moreover, there is a transition section between the γ -phase (cubic) and ϵ -phase (hexagonal) in the range from $Mn_{2.6}Ga$ to $Mn_{2.8}Ga$ (not included) [Fig. 2(b)]. To date, the arc-melted bulk cubic phase



01 October 2022 053438

FIG. 2. XRD patterns of the melt-spun ribbons of Mn–Ga alloys: (a) pure cubic region, (b) cubic + hexagonal region, and (c) pure hexagonal region. (d) The structural variation of as-cast Mn–Ga ribbons with different compositions. The insets show the lattice parameters and structural diagrams of the as-cast cubic phase and the hexagonal phase.

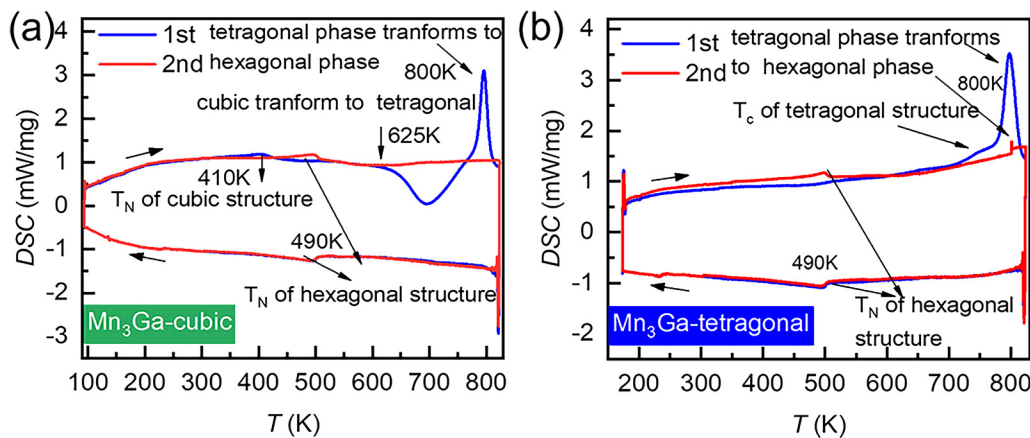


FIG. 3. DSC results of the antiferromagnetic cubic phase (a) and the ferrimagnetic tetragonal phase (b) of Mn_3Ga alloys. The heating period and cooling period are indicated by arrows, the blue curves indicate the first cycle, and the red curves indicate the second cycle.

has been reported to be obtained in the range from $\text{Mn}_{2.2}\text{Ga}$ to Mn_3Ga ,⁹ and we also obtain the cubic phase with Mn-rich compositions $\text{Mn}_{3.1}\text{Ga}$ and $\text{Mn}_{3.2}\text{Ga}$. However, for a Ga-rich composition, we obtain only mixed phases and ϵ -phase samples from $\text{Mn}_{2.8}\text{Ga}$ to $\text{Mn}_{2.3}\text{Ga}$. This is related to the difference between the cooling rates of the melt-spinning and arc-melting processes. An arc-melting sample undergoes other structural transitions during the slower cooling process. In addition, the hexagonal phase has been reported only with $\text{Mn}_{2.48}\text{Ga}$ to date.

The structural variation of the as-cast Mn-Ga ribbons with different compositions is shown in Fig. 2(d), which indicates that the structure gradually transforms from cubic to hexagonal with decreasing Mn composition. The lattice parameters of the ϵ -phase and cubic phase for different compositions are similar to those in previous studies.^{1,14} However, the lattice parameters do not seem to change regularly. The Rietveld refinement of the cubic Mn_3Ga

XRD intensity diagram shows that the lattice parameter $a = b = c = 3.7786 \text{ \AA}$, which is consistent with a former report¹ [see Fig. S1(a) in the supplementary material]. Figure 6(b) shows the selected area electron diffraction (SAED) of cubic Mn_3Ga . The SAED pattern indicates that the selected area is [011] oriented. We further confirmed the atomic arrangement along the [011] direction by STEM. A high-resolution high-angle annular dark field (HAADF) STEM image is shown in Fig. 6(a). The inset is an enlarged portion of the STEM image, and the atomic arrangement agrees with the calculated schematic atomic arrangement.

The DSC heating and cooling curves of cubic Mn_3Ga in the temperature range from 100 to 800 K for two cycles are depicted in Fig. 3(a). In the first cycle, there are two magnetic transition temperatures and two structure transition temperatures: the Néel temperatures (T_N) of the cubic phase at approximately 420 K, the cubic \rightarrow tetragonal phase at approximately 600 K, and the tetragonal

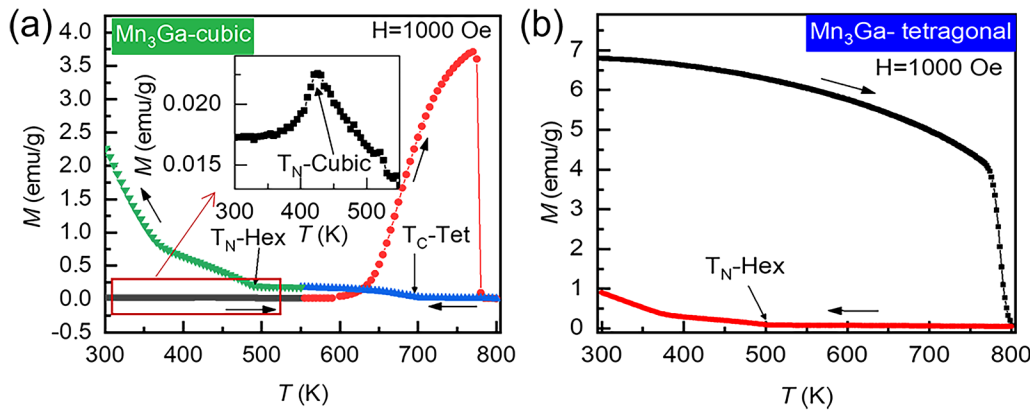


FIG. 4. Temperature dependence of magnetization $M(T)$ for the antiferromagnetic cubic phase (a) and the ferrimagnetic tetragonal phase (b) of Mn_3Ga from 300 to 800 K at 1000 Oe. The heating period and the cooling period are indicated by arrows.

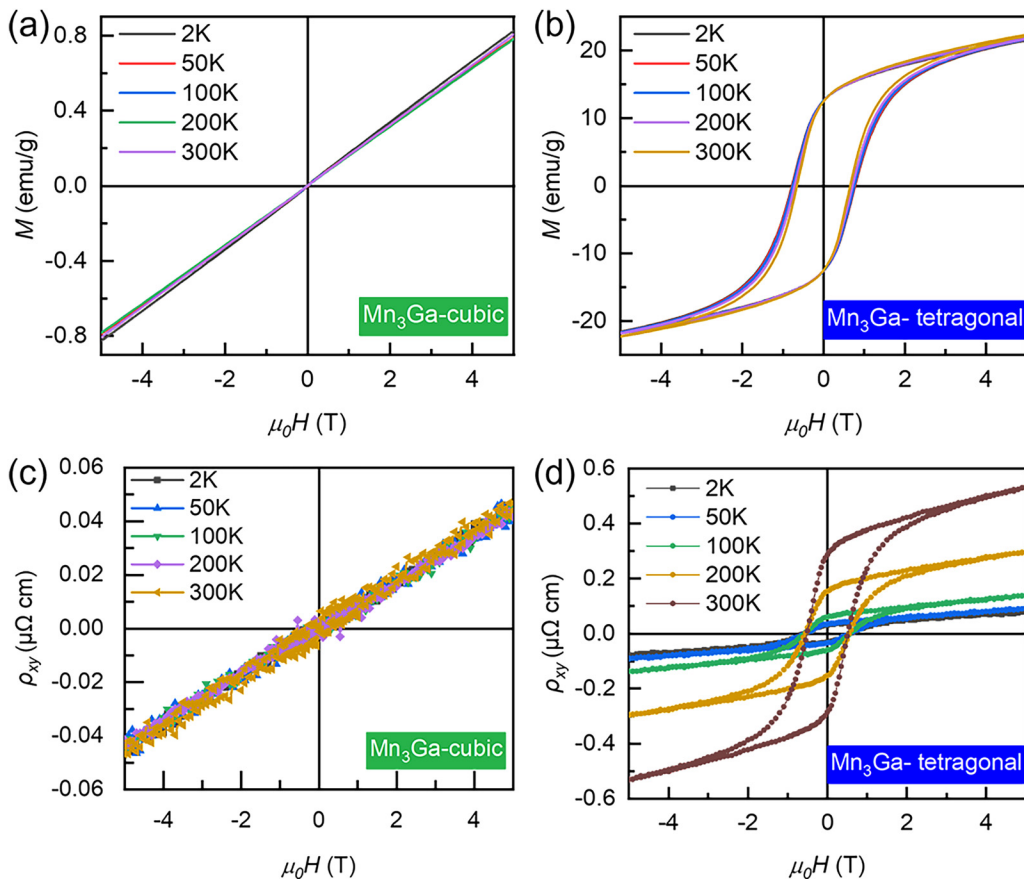


FIG. 5. The magnetic field dependence of magnetization $M(H)$ at different temperatures for the antiferromagnetic cubic phase (a) and the ferrimagnetic tetragonal phase (b) of Mn_3Ga . The magnetic field dependence of Hall resistivity (ρ_{xy}) at different temperatures for antiferromagnetic cubic (c) and ferrimagnetic tetragonal (d) Mn_3Ga .

01 October 2025 05:34:38

phase \rightarrow hexagonal phase at approximately 800 K in the heating curve and the T_N of the hexagonal phase at approximately 490 K in the cooling curve. The second cycle shows only the peaks at the T_N of the hexagonal phase in the heating and cooling curves, which means that the cubic phase has already completely transformed to the hexagonal phase and that the structural transition process is irreversible. The transition process is also supported by the temperature dependence of the magnetization $M(T)$ curves, as shown in Fig. 4(a). During the heating period, the first peak appears at approximately 420 K, which corresponds to the T_N of the cubic phase. With increasing temperature, the magnetization increases abruptly at approximately 600 K, where the γ -phase transforms to the tetragonal phase, with the paramagnetism gradually changing to ferrimagnetism. After 700 K, the magnetization increases more slowly as the transition ends. Finally, the magnetization drops to zero at approximately 800 K, while the tetragonal phase transforms to the hexagonal phase (η -phase). During the cooling period, the Curie temperature (T_C) is detected at approximately 700 K due to the rest of the tetragonal phase. Furthermore, the T_N of the hexagonal phase appears at approximately 490 K.

Then, an extra transition temperature appears at approximately 350 K. As we discuss later, this may correspond to the T_C of β -Mn. All transition processes of the γ -phase are in accordance with previous reports.¹

It should be noted that from 700 to 800 K in the heating period, the sample undergoes both a magnetic phase transition from ferrimagnetism to paramagnetism and a structural phase transition from the tetragonal phase to the hexagonal phase. The magnetization should drop to zero at approximately 700 K, at which all phases should be paramagnetic. However, the process of tetragonal phase formation requires more time to complete the transition. Thus, the large thermal hysteresis delays the paramagnetic transition temperature. In addition, the ramping rate of the temperature affects the detection of the transition process. If the ramping rate is slow enough, the entire cubic and transformed tetragonal phases will transform to the hexagonal phase. The T_C of the tetragonal phase will not be detected in the cooling period. The magnetic field dependence of magnetization $M(H)$ and the Hall resistivity $\rho_{xy}(H)$ at different temperatures for cubic phase Mn_3Ga are shown in Figs. 5(a) and 5(c), respectively. All $M(H)$ and $\rho_{xy}(H)$

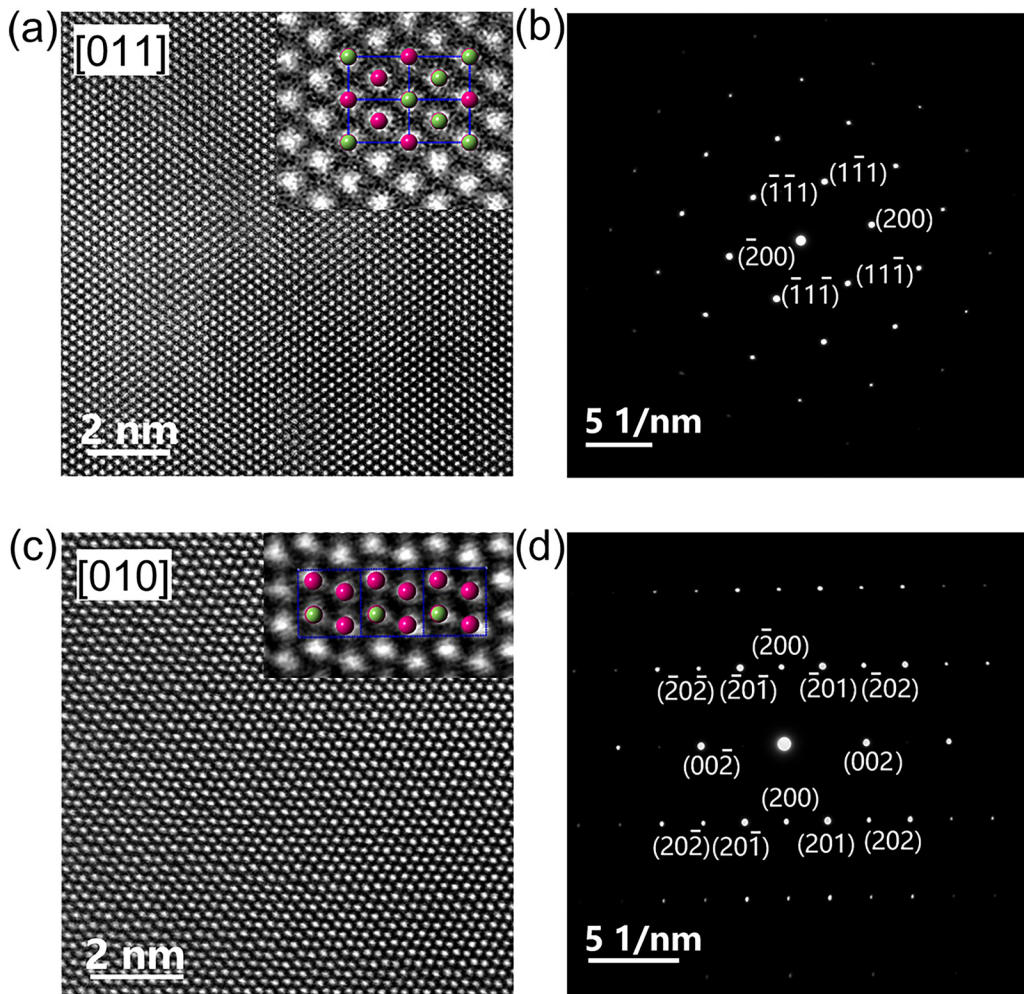


FIG. 6. High-resolution HAADF STEM images along the [011] directions of cubic Mn_3Ga (a) and along the [010] direction of hexagonal Mn_3Ga (c). The insets show expanded views. SAED patterns from cubic Mn_3Ga showing the [011] orientation (b) and hexagonal ($\text{Mn}_{2.8}\text{Ga}$) showing the [010] orientation (d).

01 October 2025 05:34:38

curves are linear, which agrees with typical collinear AFM properties.

The transition between the cubic phase and the $D0_{22}$ tetragonal phase has already been studied in detail, as mentioned above. The annealing temperature is determined by the DSC and $M(T)$ curves of the cubic phase. We annealed cubic Mn_3Ga at 350 °C for 2 weeks to obtain the tetragonal phase. The XRD intensity diagrams of the annealed sample are shown in Fig. S1(b) in the [supplementary material](#). All diffraction peaks are indexed to the $D0_{22}$ -type tetragonal structure. The Rietveld refinement of the XRD intensity diagram shows that the lattice parameters $a = b = 3.9098 \text{ \AA}$ and $c = 7.1011 \text{ \AA}$, which are similar to those in previous reports⁴ [see Fig. S1(b) in the [supplementary material](#)]. The lattice parameters a and b are similar to those of the cubic phase, and c is nearly twice as long as that of the cubic phase. The transition from the

cubic phase to the tetragonal phase seems to be an ordering process. However, for low-temperature annealed ribbons, only the $D0_{22}$ -type Mn_3Ga can be obtained, not the ordered $L1_2$ -type Mn_3Ga , which has been obtained only in films²³ thus far. The DSC heating and cooling curves of tetragonal Mn_3Ga over a temperature range from 173 to 800 K for two cycles are depicted in Fig. 3(b). In the first cycle, the T_C of the tetragonal phase appears at approximately 700 K in the heating curve. Then, a sharp peak appears at approximately 800 K that corresponds to the transition temperature from the tetragonal phase to the hexagonal phase. In the cooling curve of the first cycle, the T_N of the hexagonal phase is detected at 490 K due to the structural transition, the same as that detected in both the heating and cooling curves of the second cycle. Because the transition from the tetragonal phase to the hexagonal phase is not completed in the first cycle, the peak of the structural transition

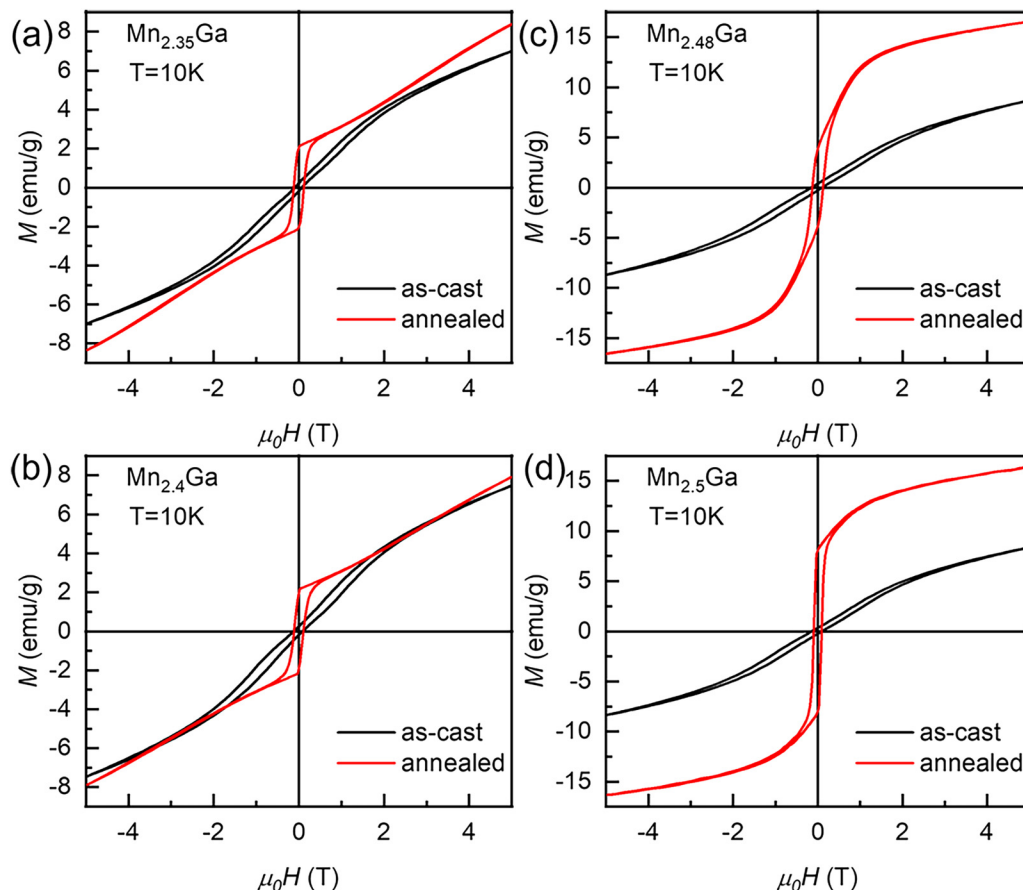


FIG. 7. The magnetic field dependence of the magnetization $M(H)$ of the noncollinear antiferromagnetic as-cast (ϵ -phase) and annealed (η -phase) hexagonal ribbons with different compositions: (a) $\text{Mn}_{2.35}\text{Ga}$, (b) $\text{Mn}_{2.4}\text{Ga}$, (c) $\text{Mn}_{2.48}\text{Ga}$, and (d) $\text{Mn}_{2.5}\text{Ga}$.

01 October 2025 05:34:38

is also detected in the second cycle. In Fig. 4(b), we show the $M(T)$ curves of the tetragonal phase from 300 to 800 K. The heating curve is similar to that in a previous report and shows the coupled magnetic and structural phase transition between the tetragonal phase and the hexagonal phase.¹⁰ The cooling curve shows the T_N of the hexagonal phase and the T_C of β -Mn at approximately 490 and 350 K, respectively. The characteristic transition temperatures of the cubic phase are not detected in the $M(T)$ curves of the tetragonal phase, which implies that the tetragonal phase we prepared is pure. The $M(H)$ and $\rho_{xy}(H)$ curves at different temperatures for tetragonal phase Mn_3Ga are shown in Figs. 5(b) and 5(d), respectively. The $M(H)$ curves show little change in the full temperature range from 2 to 300 K. Due to the large magnetocrystalline anisotropy, the coercive field is very large, similar to that in a previous report.¹⁰ The shapes of the $\rho_{xy}(H)$ curves are similar to those of the $M(H)$ curves, which implies normal transport properties. ρ_{xy} increases with decreasing temperature, which may be related to the concentration and mobility of carriers.

From the structural and magnetic transitions of the cubic and tetragonal phases, we conclude that both can transform to the

hexagonal phase—more precisely, the η -phase—above 800 K. In addition, the transition of the hexagonal phase in Mn_3Ga ribbons from the tetragonal or cubic phase separates out β -Mn, which we discuss later. In addition, the transformation between the tetragonal phase and the hexagonal phase is irreversible. Thus, we deem that ribbon samples combined with cubic and hexagonal phases [$\text{Mn}_{2.6}\text{Ga}$ to $\text{Mn}_{2.8}\text{Ga}$ (not included)] cannot transform to the pure tetragonal phase. Only the cubic part in these samples transforms to the tetragonal phase, while the hexagonal part is unchanged during the 350 °C annealing.

As we mentioned above, the ϵ -phase and η -phase are both hexagonal phases, while the exchange bias effect¹⁴ and topological Hall effect¹⁷ have been found for $\text{Mn}_{2.48}\text{Ga}$. In this work, ϵ -phase samples with different compositions were prepared, as shown in Fig. 2(c). The magnetic properties of the ϵ -phase samples should be in accordance with those reported for $\epsilon\text{-Mn}_{2.48}\text{Ga}$, which exhibits a large exchange bias effect up to room temperature. In addition, the ϵ -phase can transform to the η -phase after annealing at 600 K.¹⁴

All as-cast ribbons were annealed at 600 °C to obtain the η -phase. The XRD intensity diagrams of the η -phase of $\text{Mn}_{2.8}\text{Ga}$

TABLE I. Summarizes the results of different synthetic methods and different Mn compositions on the crystal structure of the ribbon Mn₃Ga alloys.

	As-cast	350 °C annealed	600 °C annealed
Mn _{3.2} Ga-Mn _{2.9} Ga	Cubic	Tetragonal	Hexagonal(η) + β -Mn
Mn _{2.8} Ga			
Mn _{2.6} Ga-Mn _{2.7} Ga	Cubic + Hexagonal(ε)	...	Hexagonal(η)
Mn _{2.4} Ga-Mn _{2.5} Ga	Hexagonal(ε)		
Mn _{2.3} Ga			Hexagonal(η) + γ_1 -Mn

are shown in Fig. S1(c) in the [supplementary material](#). All diffraction peaks are indexed to the D0₁₉-type hexagonal structure. The Rietveld refinement of the η -phase Mn_{2.8}Ga XRD intensity diagram shows that the lattice parameters $a = b = 5.4084 \text{ \AA}$ and that $c = 4.3547 \text{ \AA}$, similar to a former report [see Fig. S1(c) in the [supplementary material](#)]. Figure 6(d) shows the SAED of η -phase Mn₃Ga. The SAED pattern indicates that the selected area is [010] oriented. We further confirmed the atomic arrangement along the [010] direction by STEM. A high-resolution HAADF STEM image is shown in Fig. 6(c). The inset shows an enlarged portion of the STEM image, and the atom arrangement agrees with the calculated schematic atomic arrangement. As shown in Fig. S2(d) in the [supplementary material](#), only the ribbons with Mn compositions ranging from approximately 70 to 75 at. %—namely, Mn_{2.35}Ga to Mn_{2.8}Ga—can transform to the pure η -phase, which agrees with the boundary of the η -phase region in the Mn-Ga phase diagram. In Mn-rich ribbons, such as Mn₃Ga and Mn_{2.9}Ga, β -Mn is separated during the annealing process [see Fig. S2(a) in the [supplementary material](#)]. In the Ga-rich ribbons beyond the region of the η -phase, such as Mn_{2.3}Ga, γ_1 -Mn is separated [see Fig. S2(c) in the [supplementary material](#)] during the annealing process. Thus, the extra magnetic transition at approximately 350 K in the M(T) curves of the cubic and tetragonal phases should correspond to the T_C of β -Mn. In addition, we tried to anneal the Mn₃Ga ribbons with the different annealing paths. However, the pure hexagonal sample still could not be obtained. [See Fig. S2(b) in the [supplementary material](#)]. It can be concluded that hexagonal Mn₃Ga can be obtained only in Ga-rich compositions. It is worth noting that the transition of the η -phase we discussed above is applicable only to ribbons. We also annealed the arc-melted bulk at 600 °C for 1 week. Although there is a hexagonal phase transition in the bulk, the annealed bulk is mixed with other phases (see Fig. S3 in the [supplementary material](#)). The large internal stress with higher energy originating from the melt-spinning process may promote the structural transition in the ribbons.

Obviously, the ε -phase and η -phase exhibit isomorphic heteromagnetism. Figure 7 shows the M(H) curves of the as-cast (ε -phase) and annealed (η -phase) hexagonal ribbons of different compositions at 10 K. After annealing, the magnetization is enhanced. In addition, interestingly, the shapes of the η -phase M(H) curves of the Mn-rich samples and Ga-rich samples are distinct, which implies that there are some other properties in the η -phase for different compositions in addition to the crystal distortion and topological Hall effect found in η -Mn_{2.48}Ga.¹⁷ The M(H) curves of the Ga-rich samples show an extra magnetizing transformation at approximately 2 T, as shown in Figs. 7(a) and 7(b), while

the M(H) curves of the Mn-rich samples show FM-like shapes due to spin canting from in-plane to out-of-plane, as shown in Figs. 7(c) and 7(d). The results of different Mn compositions on the crystal structure of the ribbon Mn₃Ga alloys are summarized in Table I. The properties of the η -phase should exhibit regular variation as the composition of Mn changes, which we are currently studying.

IV. SUMMARY

We obtained three different phases of Mn₃Ga alloys with Mn compositions ranging from approximately 70 to 75 at. % and systematically investigated their structural, magnetic, and transport properties. The disordered L1₂ cubic phase and the hexagonal (ε -phase) phase could be directly obtained by rapid melt-spinning. We found that the cubic phase can transform to the D0₂₂ tetragonal phase by postannealing. Through the thermodynamic and magnetic properties of the cubic and tetragonal phases, we found that both can transform to the hexagonal η -phase. In addition, this was the first time that isomeric heteromagnetism hexagonal phases (ε -phase and η -phase) of Mn₃Ga were clearly distinguished by magnetism and the preparation method. The η -phase with different compositions showed more interesting magnetic properties that should be further studied. This work will promote in-depth research on Mn-Ga alloy systems and their application in AFM spintronics with topological properties.

SUPPLEMENTARY MATERIAL

See the [supplementary material](#) for the XRD patterns of different structures of Mn₃Ga ribbon alloys (Fig. S1), the discussion of the η -phase formation of the samples with the composition around the boundary of the η -phase region (Fig. S2), and the discussion of the formation of arc-melt bulk Mn-Ga alloys (Fig. S3).

ACKNOWLEDGMENTS

This work was supported by the National Key R&D Program of China (No. 2021YFB3501402) and the National Natural Science Foundation of China (NNSFC) (No. 11974406).

AUTHOR DECLARATIONS

Conflict of Interest

The authors have no conflicts to disclose.

Author Contributions

L.S. contributed to resources, investigation, writing—original draft, and data curation. B.D. contributed to investigation and data curation. H.L. contributed to investigation and data curation. S.L. contributed to visualization and data curation. Y.Y. contributed to investigation and data curation. D.Z. contributed to supervision and methodology. J.H. contributed to supervision, writing-review and Editing, and methodology. W.W. contributed to conceptualization, methodology, writing—review and editing, supervision, and funding acquisition.

DATA AVAILABILITY

The data that support the findings of this study are available from the corresponding authors upon reasonable request.

REFERENCES

- ¹P. Kharel, Y. Huh, N. Al-Aqtash, V. R. Shah, R. F. Sabirianov, R. Skomski, and D. J. Sellmyer, *J. Phys.: Condens. Matter* **26**(12), 126001 (2014).
- ²H.-W. Bang, W. Yoo, C. Kim, S. Lee, J. Gu, Y. Park, K. Lee, and M.-H. Jung, *Appl. Phys. Lett.* **115**(1), 012402 (2019).
- ³H. Niida, T. Hori, H. Onodera, Y. Yamaguchi, and Y. Nakagawa, *J. Appl. Phys.* **79**(8), 5946 (1996).
- ⁴E. Krén and G. Kádár, *Solid State Commun.* **8**(20), 1653 (1970).
- ⁵K. Minakuchi, R. Y. Umetsu, K. Ishida, and R. Kainuma, *J. Alloys Compd.* **537**, 332 (2012).
- ⁶J. Winterlik, B. Balke, G. H. Fecher, C. Felser, M. C. M. Alves, F. Bernardi, and J. Morais, *Phys. Rev. B* **77**(5), 054406 (2008).
- ⁷D. Liang, G. Tian, C. Yun, H. Zhao, S. Liu, C. Wang, J. Han, H. Du, Q. Xu, Y. Zhang, J. Yang, and W. Yang, *Appl. Phys. Lett.* **119**(2), 022403 (2021).
- ⁸H. Zhao, W. Yang, Z. Shao, G. Tian, D. Zhou, H. Du, S. Liu, J. Han, C. Wang, J. Xu, D. Yu, Y. Yang, and J. Yang, *Scr. Mater.* **129**, 6 (2017).
- ⁹J. Z. Wei, R. Wu, Y. B. Yang, X. G. Chen, Y. H. Xia, Y. C. Yang, C. S. Wang, and J. B. Yang, *J. Appl. Phys.* **115**(17), 17a736 (2014).
- ¹⁰B. Balke, G. H. Fecher, J. Winterlik, and C. Felser, *Appl. Phys. Lett.* **90**(15), 152504 (2007).
- ¹¹S. Wurmehl, H. C. Kandpal, G. H. Fecher, and C. Felser, *J. Phys.: Condens. Matter* **18**(27), 6171 (2006).
- ¹²H. Kurt, K. Rode, M. Venkatesan, P. Stamenov, and J. M. D. Coey, *Phys. Rev. B* **83**(2), 020405(R) (2011).
- ¹³X. S. Lu, J. K. Ling, and M. G. Zhou, *Acta Phys. Sin.* **29**, 469 (1980).
- ¹⁴L. Song, B. Ding, H. Li, S. Lv, Y. Yao, D. Zhao, J. He, and W. Wang, *J. Magn. Magn. Mater.* **536**, 168109 (2021).
- ¹⁵S. Nakatsuji, N. Kiyohara, and T. Higo, *Nature* **527**(7577), 212 (2015).
- ¹⁶G.-Y. Guo and T.-C. Wang, *Phys. Rev. B* **96**(22), 224415 (2017).
- ¹⁷L. Song, B. Ding, H. Li, S. Lv, Y. Yao, D. Zhao, J. He, and W. Wang, *Appl. Phys. Lett.* **119**(15), 152405 (2021).
- ¹⁸Z. H. Liu, Y. J. Zhang, G. D. Liu, B. Ding, E. K. Liu, H. M. Jafri, Z. P. Hou, W. H. Wang, X. Q. Ma, and G. H. Wu, *Sci. Rep.* **7**(1), 515 (2017).
- ¹⁹H. Kurt, K. Rode, H. Tokuc, P. Stamenov, M. Venkatesan, and J. M. D. Coey, *Appl. Phys. Lett.* **101**(23), 232402 (2012).
- ²⁰F. Hu, G. Z. Xu, Y. R. You, Z. Zhang, Z. Xu, Y. Y. Gong, E. Liu, H. G. Zhang, E. K. Liu, W. H. Wang, and F. Xu, *J. Appl. Phys.* **123**(10), 103902 (2018).
- ²¹B. B. Singh, K. Roy, J. Arout Chelvane, and S. Bedanta, *Phys. Rev. B* **102**(17), 174444 (2020).
- ²²S. Khmelevskyi, A. V. Ruban, and P. Mohn, *Phys. Rev. B* **93**(18), 184404 (2016).
- ²³H.-W. Bang, W. Yoo, K. Lee, Y. H. Lee, and M.-H. Jung, *J. Alloys Compd.* **869**, 159346 (2021).